Lasers in Manufacturing Conference 2021

Temporally and spatially highly resolved reconstruction of vapor capillary geometry during laser beam welding using synchrotron radiation

Marc Hummel[a,*], André Häusler[b], Sören Hollatz[b], Christian Hagenlocher[c], Jannik Lind[c], Ulrich Halm[d], Christoph Schöler[d], Alexander Olowinsky[b], Arnold Gillner[a,b]

[a]RWTH Aachen University. Chair for Laser Technology LLT, Steinbachstraße 15, 52074 Aachen, Germany
[b]Fraunhofer-Institute for Laser Technology ILT, Steinbachstraße 15, 52074 Aachen, Germany
[c]Institut für Strahlwerkzeuge, University of Stuttgart, Pfaffenwaldring 43, 70569 Stuttgart, Germany
[d]RWTH Aachen University, Nonlinear Dynamics of Laser Processes NLD, Steinbachstraße 15, 52074 Aachen, Germany

Abstract

Welds of electrical components made of aluminium and copper need high electrical and mechanical quality. Process instabilities do not allow a continuous reproducibility. To generate a deeper understanding of the process and to evaluate process dynamics, it is possible to use modern in situ analysis methods.

In this work, in situ phase-contrast high-speed videography using synchrotron radiation is presented. The phase contrast method reveals the phase boundaries between solid, liquid, and gaseous phases. A spatial resolution down to < 20 μm is possible due to the high coherence of the synchrotron beam, which allows to observe small vapor capillaries of fiber lasers with < 100 μm diameter. 3D capillary geometries are reconstructed from 2D image data of welds on aluminium using a fibre laser and disc laser. Ray tracing is performed using this reconstruction, which allows the time resolved tracking of the laser beam inside the vapor capillary for quantitative estimations.

Keywords: synchrotron; laser welding; vapour capilarry dynamic; reconstruction;

* Corresponding author. Tel.: +49 241 8906-8198
E-mail address: marc.hummel@llt.rwth-aachen.de

1. Introduction

A paramount challenge in laser micro welding is to design welding processes both highly energy efficient and precise regarding weld depth and surface roughness. With society's increasing interest in alternative energy storage systems, the demand for highly conductive battery connectors and light weight structures increases and processes for contacting electronic components for batteries and fuel cells are gaining in importance. Fibre and disc lasers with a wavelength in the near infrared range (1030-1070 nm) have established themselves for this purpose [1,2]. However, the high thermal conductivity and low energy absorption of infrared radiation on aluminium cause instabilities during the welding process and lead to significant difficulties such as process and pore and spatter formation.

A conventional high-speed X-ray imaging system, such as implemented at the IFSW in Stuttgart to investigate the fundamentals of laser material processing, is a possible option for investigations. This system consists of a microfocus X-ray tube, a scintillator, an image intensifier, and a conventional high-speed camera. It enables the resolution of 200 μm objects at a frame rate of 1 kHz, which was suitable for many different investigations of laser welding processes [3,4]. The limits of the spatial and temporal resolution of the system are given by the edge blurring created by the aperture of the X-ray source and the noise caused by the image intensifier due to the small number of photons generated by the X-ray tube. In addition, a contrast between the solid and liquid physical state is not visible. These limits can be overcome by using a high brilliance X-ray spectrum generated by a synchrotron source. By X-ray phase-contrast imaging the phase boundaries solid-liquid and liquid-gaseous become visible [5,6].

In this work, the possibilities offered by using synchrotron radiation as a tool for analysing laser welding process is presented. The high speed in situ phase contrast videos of aluminum are used to reconstruct the geometry of vapor capillaries produced with fibre and disc lasers. A raytracing algorithm is used to predict the energy distribution in the keyhole. Finally, a reconstructed weld seam longitudinal section from the videos is compared to a metallographic cross section with means of pore formation and the surface profile.

2. Experimental Setup

In this work laser beam welding of aluminum with both a disc and fibre laser are investigated in the high energy beamline P07 (EH4) of Petra 3 at the Deutsches Elektronen-Synchrotron DESY in Hamburg [7]. For this application, a customised experimental setup for Beamline P07 was developed at the Chair of Laser Technology at RWTH Aachen University and the Fraunhofer Institute for Laser Technology ILT. With this setup, all types of laser material processing can be realised. The part of the optical setup including the high speed axis is shown in Figure 1.
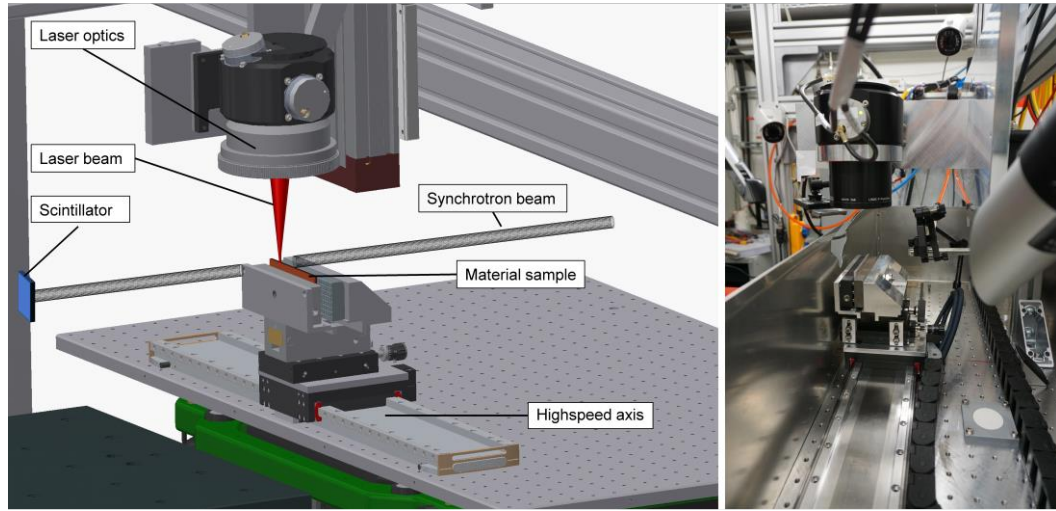
Fig. 1. Experimental setup for phase contrast observation of laser welds; left: CAD-Model; right: real setup

A Linax Lxs electromagnetic high-speed axis from Jenny Science was used to travel the material through the intersection of the laser and the synchrotron beam. The maximum speed of the axis is set to 2000 mm/s. The used Scintillator was a $CdWO_4$ (Cadmiumwolframat) material with an area of 11x11 mm^2 and a thickness of 300 µm. The scintillator is used as the detector for the synchrotron radiation and is illuminated depending on the intensity of the synchrotron beam. The illuminating scintillator was filmed from the backside inside of an optical tower of the beamline with optimum surrounding darkness. For high speed acquisition of the image data a Photron Fastcam SA5 was implemented inside the optical tower. The camera was set to 1024 x 768 pixel and a frame rate of 1 kHz with an exposure time of 1 ms.
For the experiments, the following beamline parameters are used, as presented in table 1.

Table 1. Synchrotron setup and parameters for the investigation

Parameter	Unit	P07 Petra 3
Operation Mode	[-]	Low Beta
Photon energy	[keV]	37,7
Beam area	[mm²]	2x2
Scintillator material	[-]	CdWO₄
Scintillator size	[mm²]	11x11
Scintillator thickness	[µm]	300
Distance scintillator – material sample	[mm]	800

For the experiments, the following laser beam sources are used as presented in table 2:

Table 2. Laser beam sources used for the investigations

Parameter	Unit	IPG YLR-2000WC	Trumpf TruDisk 5001
Wavelength	[nm]	1070	1030
Laser power (max.)	[W]	2000	5000
Fibre diameter	[µm]	18	50
Focal length collimator	[mm]	70	80
Focal length optics	[mm]	163	163
Focal diameter (measured)	[µm]	34.3	117.3

The labels and process parameters of the investigated experiments are summarized in table 3. Note that the laser power is constant for each laser source and only the feed rate is varied. The difference in laser power results from the different focal diameters of both beams (c.f. table 2). The parameters are selected in order to achieve a sufficient capillary depth that can still be imaged on the camera sensor and, on the other hand, line energies that show an overlap for both laser beam sources. The laser beam intensities in the focus differs by a factor of ~3.

Table 3. Process parameters and labels of investigated experiments

Label	Laser source	Laser power [W]	Feed rate [mm/s]
I500-200			200
I500-300	IPG YLR-2000WC	500	300
I500-400			400
T2000-600			600
T2000-800	Trumpf TruDisk 5001	2000	800
T2000-1000			1000

3. Data Acquisition and Evaluation

By the high-speed camera a sequence of image files with photon counts (scintillator intensities) is recorded during each experiment. These images represent a discrete time series evaluated at locations sequentially displaced by v/f relative to the material, where v and f are the feed rate of the material and the frame rate of the camera, respectively. The raw image data are further processed to obtain different information on the process as described in the following. First, a shading algorithm is applied to all raw images to improve overall image quality by reducing background noise and vignetting by the X-ray beam. Furthermore, image contrast is increased by adjusting the colour space of the images.[8]

For high-speed video generation and 3D reconstruction of keyhole geometries, a moving temporal median filter is applied. Thus, the contrast between phase boundaries is greatly enhanced, albeit suppressing the observation of process features on short time scales. The number of image frames that are used by the filter is set to five during video generation for being able to observe pore formation, whereas during 3D keyhole reconstruction 50 frames are averaged for a higher contrast between the liquid and gaseous phase boundaries.

For the 3D reconstruction of keyhole surfaces the method by Lind et al. [9] is adopted. Information regarding length and depth of the geometric shape of the keyhole is directly extracted from the processed X-ray images by feature detection mechanisms. Information about the keyhole width (perpendicular to the image plane) is obtained by evaluation of grey values and interpolation against reference values obtained from borehole measurements (c. f. [9]). Due to unneglectable image noise the grey values are averaged over the pixel columns to determine an average keyhole width per pixel row. The geometric shape of the keyhole surface in the horizontal is assumed as elliptical with minor axes corresponding to these average widths.

For the reconstruction of longitudinal sections areas behind the melt pool (ROI) from single images with 1kHz repetition rate are stacked together side by side for evaluation of pores and surface roughness. This method is schematically shown in Figure 2.
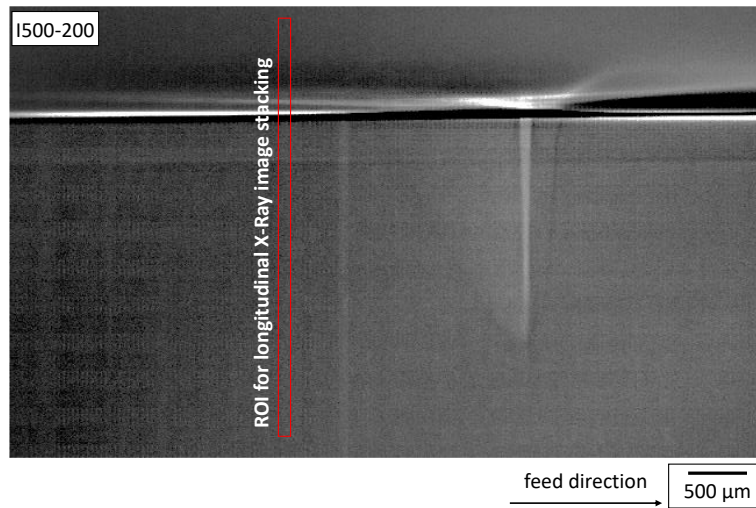

Fig. 2. longitudinal image stacking for reconstruction of a weld seam from tomography images

For the evaluation an image scale of 262 pixel/mm is used. The width of the ROI is adjusted to the feed rate of the process parameter (52 to 262 pixel). The height remains constant. The limitation of the evaluation method used is given by the maximum exposure time achieved. At 200 mm/s, for example, the sample moves 200 µm (52 pixels) during one image. As the feed rate increases, the edges of the pores, surface and fusion line become more indistinct due to dynamic blurring.

4. Results and Discussion

The methods presented in this paper are first demonstrated using a time series of the recording T2000-600 as an example. These are shown in Figure 3. Each image is recorded with the exposure time of 1 ms.
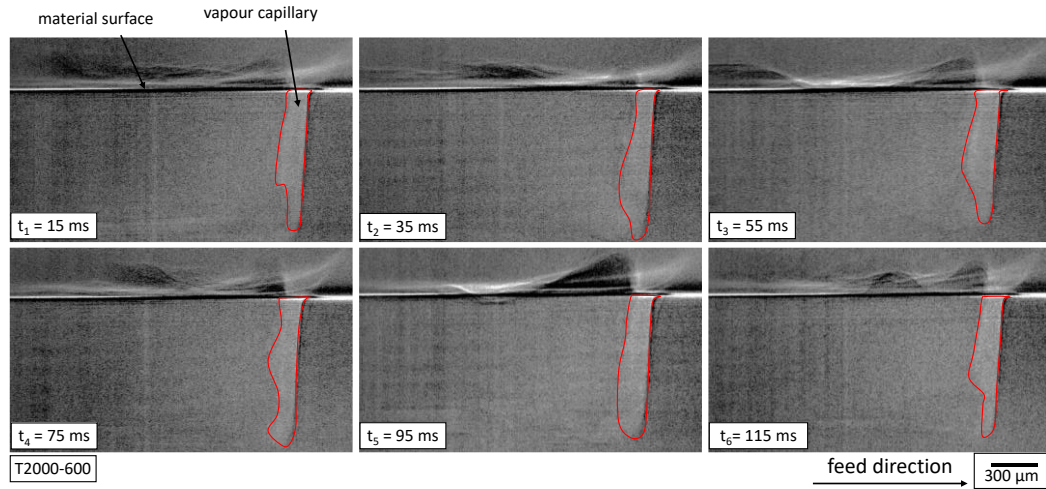
Fig. 3. Temporally resolved welding process with visible phase boundaries

The material surface and the vapour capillary can be seen. The phase contrasts are traced to ensure better visibility. The phase contrast of the melt pool is only slightly visible because of the high feed rate of 600 mm/s and the exposure time of 1 ms, which results in a dynamic noise in the image. For parameters with lower feed rates, these are easier to recognise. The macroscopic fluctuations in the images from image to image are clearly visible. The surface structure of the melt in the liquid and solidified phase is also visible. This allows a later inference of the internal processes of the process to the final surface roughness.

For a qualitatively better evaluation between the parameter sets and laser beam sources, 50 images of each parameter set are averaged by means of a median filter. This makes the contrasts between the phases more apparent. These images are presented in Figure 4.
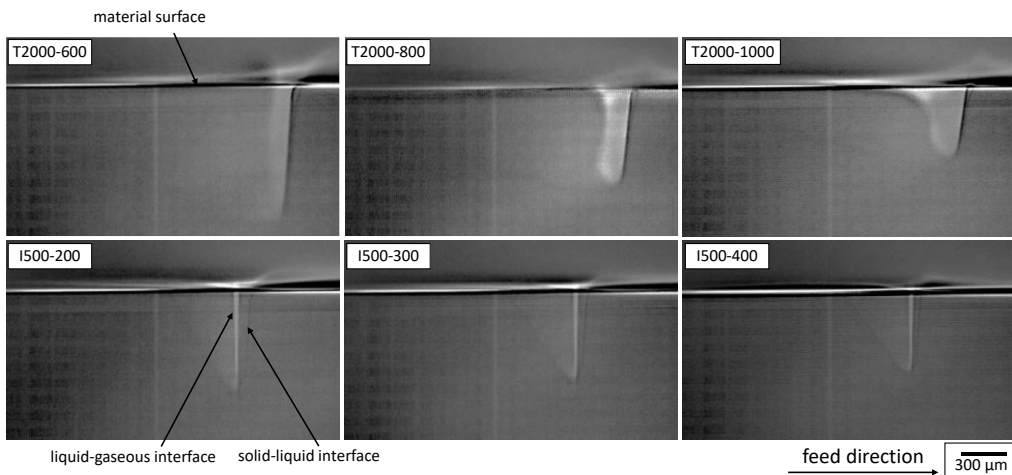

Fig. 4. Comparison of vapour capillary and *melt* pool geometry depending of laser beam source and laser parameters

The first thing that catches the eye is the different aspect ratio. While the welds with the Trumpf disc laser show a longitudinal aspect ratio (length to depth of the keyhole) of 5.08, 2.46 and 0.74, the welds with the IPG fibre laser show aspect ratios of 12.79, 12.84 and 12.66. Thus, the aspect ratio changes for the disc laser with increasing speed by a factor of 6.9 while the aspect ratio of the fibeer laser welds remains constant. In addition, the changing shape of the capillary with increasing feed rate is clearly visible with the disc laser (T2000-1000). As the feed rate increases, the capillary opens at the top and the welding depth decreases. The advantage of this is a more stable process with less pore formation.

If the sensitivity of the capillary depth to the feed rate is compared between the Trumpf disc laser and the IPG fibre laser, a further difference becomes apparent. The sensitivity (delta of the welding depth/delta of the feed

rate) is 1.15 $\mu m / mm/s$ for the Trumpf disc laser and 0.66 $\mu m / mm/s$ for the IPG fibre laser. The sensitivity of the fibre laser to a change in feed rate, which is lower by a factor of 2, can be particularly advantageous in welding applications with spatial power modulation (wobbling), since a change in path speed would result in smaller deviations in the welding depth.

From the images in the top row in Figure 4 three-dimensional shapes of the keyhole surfaces have been extracted for an analysis of the distribution of the absorbed laser intensity by a raytracing algorithm. For this, an experimental characterization of the intensity profile of the Trumpf TruDisk 5001 laser beam was performed. The propagation characteristics of the beam within the propagation distance of interest and the beam profile in the focal plane are depicted in Figure 5. The beam profile shows a slight asymmetry with respect to the optical axis. From the beam profile measurement and the operating value of the laser power $P_L = 2000$ W a maximum intensity of $I_0 \approx 4 \times 10^{11}$ W/m^2 was calculated.
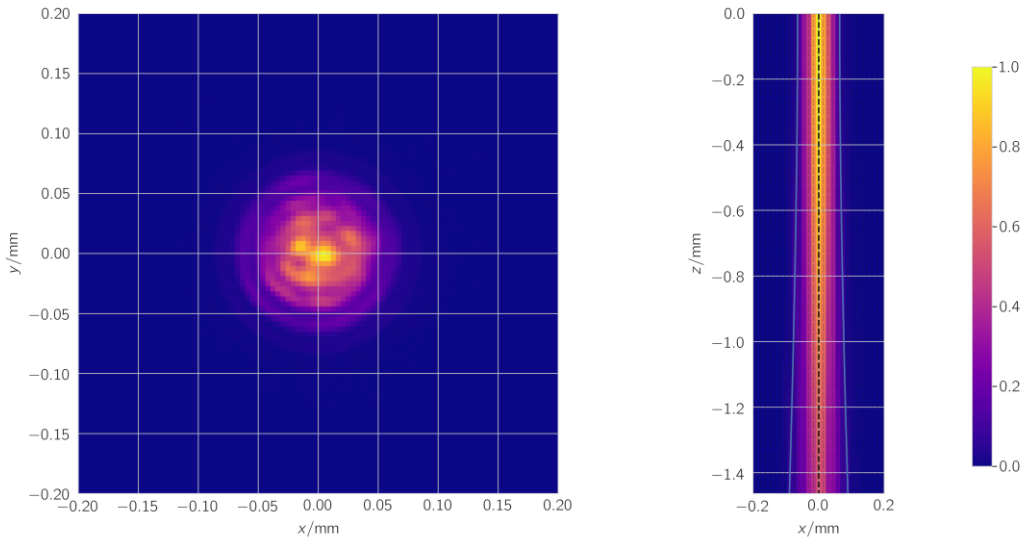

Fig. 5. Measured beam profile in the focal plane $z = 0$ (left) and in the plane $y = 0$ (right) with intensity values scaled to the maximum intensity for the disc laser TruDisk 5001.

During raytracing, the Fresnel curves of aluminium are considered to compute the fraction of absorbed power as a function of the angle of incidence. For the optical constants $n = 3.028$ and $k = 8.796$ are used, which correspond to measured values at a temperature of 1173 K at a wavelength of 1030 nm [10]. Furthermore, unpolarized light is assumed and the position of the optical axis with respect to the keyhole's front position is parameterized as "axis offset" since it could not be reliably obtained from our reference measurements.

Figure 6 shows a result of the raytracing calculations for three different feed rates. With increasing feed rate the distribution of the absorbed intensity becomes more uniform along the keyhole front. Lower irradiation isvisible at the sides of the keyhole surface. This might be an indicator for the increased process stability that is observed at higher feed rates as shown in Fetzer et al. [11]. For the highest feed rate, the rear part of the keyhole near the workpiece top is hardly illuminated by laser light which might be an effect of the melt flow. Moreover, a variation of the axis offset only showed a minor influence on the spatial intensity distribution which is exemplified in Figure 7.
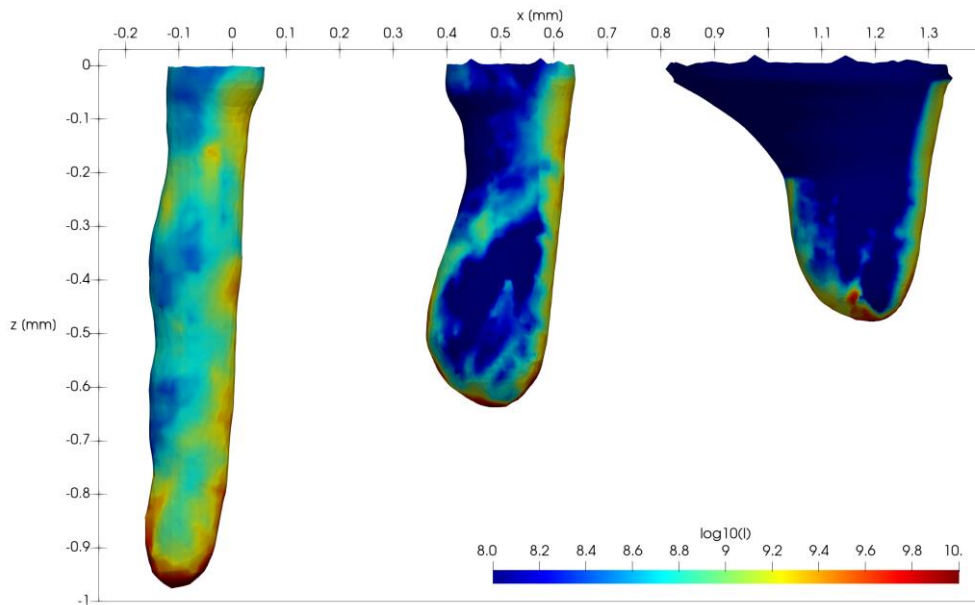

Fig. 6. Comparison of absorbed intensities *I* on reconstructed three-dimensional keyhole surfaces computed by raytracing for the parameters T2000-600 (left), T2000-800 (center), T2000-1000 (right) with optical axes positioned at x = 0, 0.6, 1.3, respectively.
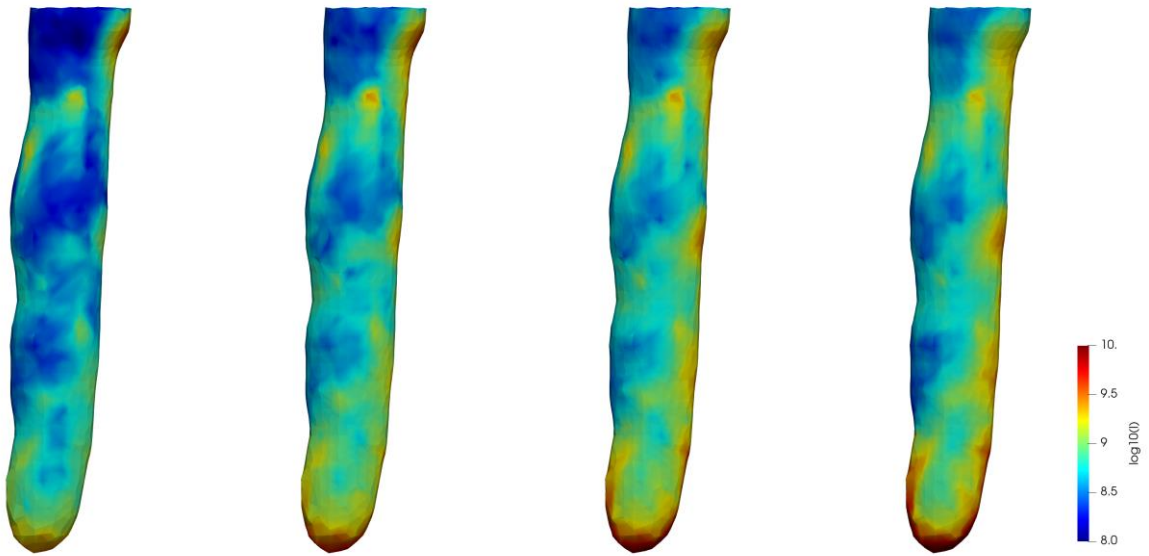
Fig. 7. Distribution of the absorbed intensity *I* on the reconstructed three-dimensional keyhole surface of parameter set T2000-600 for axis offsets 0, 20, 40, and 60 µm (from left to right).

In Figure 9 the comparison of a metallographic longitudinal section of the I500-200 weld seam with a longitudinal section composed from the tomographic data is presented. It additionally shows the possibility of examining both the final surface structure and the pores formed inside the weld seam from the dynamic process data without the need for a new X-ray image of the finished weld seam. The gap in the metallographic longitudinal section results from a required separation of the long sample into shorter segments and could not be avoided
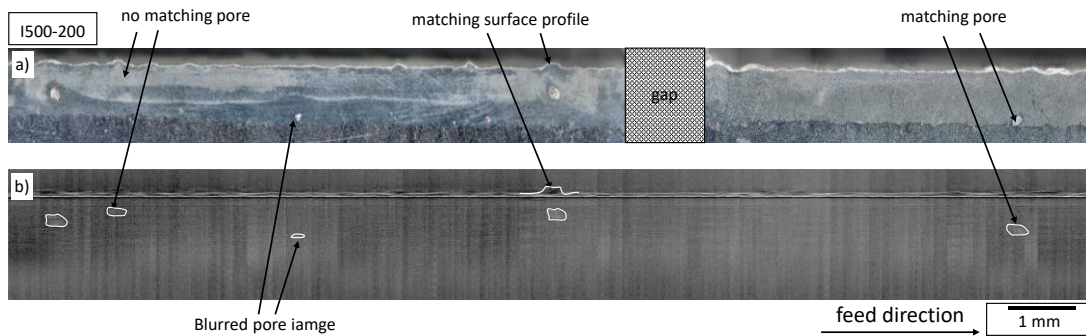

Fig. 9. Comparison between longitudinal section between a) metallographic and b) tomographic data

The composition of this tomographic longitudinal section can be carried out in quasi-real time using a suitable algorithm. The position of surface structures and the pores correspond very precisely to the real longitudinal section. In addition, it can also be seen in the left-hand area of the weld that a pore is visible in the tomographic image that is not visible in the metallographic longitudinal section. This is caused by the detection of the entire spatial depth of the weld by the X-ray beam. This means that pores can also be detected

which lie outside the metallographic section plane and shows a clear advantage over metallographic evaluations.

The shape of the pores is however noticeably displayed longer in the tomography images in this example. This is due to the long exposure time of the high-speed camera of 1 ms and will be addressed again in future experiments.

5. Conclusions and Outlook

The presented investigations show an overview of the possibilities for analyzation with high brilliant synchrotron laser beam sources. Beside the image acquisition, additional reconstruction of the 3D keyhole, raytracing and the 2D longitudinal section was presented. The following conclusions can be drawn:

1) High speed phase contrast images of laser welding processes allow the detailed observation of the dynamic processes inside the capillary and the melt pool.
2) Digital image processing combined with the borehole method enable a 3D reconstruction of the keyhole surfaces that can be employed in further numerical analyses.
3) Raytracing can be used for the qualitative and quantitative analyses of the energy distribution onside the keyhole and can provide insightful information about mechanisms affecting process stability.
4) The longitudinal sections obtained from a streak analysis of single images is more detailed and allows the observations of pores in the total depths of the weld seam compared.
5) Welds with fiber lasers show a lower sensitivity of the keyhole depths on the feed rate by a factor of 2 compared to the welds with disc lasers.

In future investigations, the focus is set on the time resolved raytracing for the more detailed analysis of the pore formation in laser welding processes. For a microscopic observation of the processes on the capillary surface and in the melt pool, the temporal as well as the spatial resolution should be further increased in the experiments. Additionally, a cross check should be carried out between sensitivity of the keyhole depth, the keyhole stability, and the aspect ratio of the keyhole.

References

[1]   A. Häusler, et al., Efficient copper microwelding with fibre lasers using spatial power modulation, Lasers in Engineering 36 (2017) 133–146.
[2]   F. Schmitt, Laserstrahl-Mikroschweißen mit Strahlquellen hoher Brillanz und örtlicher Leistungsmodulation. Dissertation, Aachen, 2012.
[3]   A. Heider, et al., High-Speed X-Ray Analysis of Spatter Formation in Laser Welding of Copper, Physics Procedia 41 (2013) 112–118. https://doi.org/10.1016/j.phpro.2013.03.058.

[4]   F. Fetzer, et al., Reduction of pores by means of laser beam oscillation during remote welding of AlMgSi, Optics and Lasers in Engineering 108 (2018) 68–77. https://doi.org/10.1016/j.optlaseng.2018.04.012.

[5]   Y. Kawahito, H. Wang, In-situ Observation of Laser Manufacturing with X-ray Technique, Synchrotron Radiation News 32 (2019) 14–19. https://doi.org/10.1080/08940886.2019.1582283.

[6]   M. Miyagi, et al., X-ray phase contrast observation of solidification and hot crack propagation in laser spot welding of aluminum alloy, Opt. Express 26 (2018) 22626–22636.

[7]   N. Schell, et al., The High Energy Materials Science Beamline (HEMS) at PETRA III, MSF 772 (2013) 57–61. https://doi.org/10.4028/www.scientific.net/MSF.772.57.

[8]   F. Abt, et al., X-ray videography for investigation of capillary and melt pool dynamics in different materials, ICALEO 2011 (2011) 179–186. https://doi.org/10.2351/1.5062233.

[9]   J. Lind, et al., Transition from Stable Laser Fusion Cutting Conditions to Incomplete Cutting Analysed with High-speed X-ray Imaging, Journal of Manufacturing Processes 60 (2020) 470–480. https://doi.org/10.1016/j.jmapro.2020.10.068.

[10]   L.A. Akashev, V.I. Kononenko, Optical Properties of Liquid Aluminum and Al–Ce Alloy, High Temperature 39 (2001) 384–387. https://doi.org/10.1023/A:1017502424054.

[11]   F. Fetzer, et al., Pores in laser beam welding: generation mechanism and impact on the melt flow, Conference Proceedings of SPIE LASE 105250 D (2018) 12. https://doi.org/10.1117/12.2295798.